EES Batteries

PAPER

View Article Online
View Journal | View Issue

Cite this: *EES Batteries*, 2025, **1**, 1583

Key factors influencing the plateau region in N-doped hard carbon for sodium storage

Xingqi Chang,[a,b] Xiaolong Zhou,*[c] Pornsuwan Buangam,[d] Nuntaporn Kamonsutthipaijit,[d] Sarayut Tunmee[d] and Andreu Cabot *[a,e]

Hard carbon (HC) is a promising anode material for the commercialization of sodium-ion (Na^+) batteries (SIBs) due to its abundant resources, low voltage plateau, and high reversible capacity. The Na^+ storage mechanism in HC can be categorized into adsorption, intercalation, and filling models. However, establishing a direct correlation between Na^+ storage and HC architecture remains challenging due to the extremely difficult control of the HC structure during synthesis. To better understand the Na^+ storage mechanism within HC, key factors such as specific surface area, heteroatom doping, and pore architecture must be carefully investigated. In this study, we synthesize nitrogen and oxygen co-doped HC nanosheets with negligible micro- and mesoporous structures and a low specific surface area, approaching the ideal "house of cards" model. This model sample allows for gaining insights into the Na^+ electrochemical behavior. By combining *in situ* X-ray diffraction, *ex situ* Raman spectroscopy, and wide/small-angle X-ray scattering, we demonstrate a clear correlation between defect sites and electrochemical behavior in the slope region, and an expanded plateau region. We propose a dominant layer-filling mechanism to explain Na^+ storage in the plateau region, attributing it to the filling of disordered carbon layers rather than the filling of nano-/micro-pores. Additionally, we demonstrate that the defect-adsorption behavior is highly influenced by the compactness of the carbon layer structure. This work offers a fresh perspective on Na^+ storage and provides valuable insights for the rational design of high-performance HC anodes in SIBs.

Received 10th September 2025,
Accepted 29th September 2025

DOI: 10.1039/d5eb00168d

rsc.li/EESBatteries

Broader context

With the advancement of the sodium-ion battery (SIBs) market, the corresponding anode electrode materials have emerged as a critical concern in the progression of SIB technology. Among the alternative anode materials, hard carbon (HC) is distinguished by its disordered and randomly graphitized structure, providing a specific capacity of approximately 300 mAh g^{-1} and a low output voltage of ~0.2 V. Due to the intricate structure of natural materials, the Na^+ storage mechanism of HC remains contentious, significantly limiting the development of SIBs. Consequently, current studies frequently deviate from the ideal 'house of cards' model for HC anodes, which envisions randomly stacked graphene layers and is vital for comprehending key storage processes. Furthermore, despite substantial advancements, the debate persists, emphasizing the need for a more comprehensive understanding of Na^+ storage mechanisms. In this study, we investigated the sodium storage mechanism in a carbon system that follows the "house of cards" model, revealing that the slope/plateau-region capacity is predominantly independent of nanopore distribution or surface area, relying instead on intrinsic micro-/meso-structural characteristics through a layer-filling mechanism. This finding highlights that merely increasing surface area or introducing nanopores does not significantly enhance plateau-region capacity *via* this mechanism. Rather, optimizing precursor materials and carbonization techniques emerges as a more effective strategy.

1. Introduction

Sodium-ion batteries (SIBs) have emerged as a promising alternative to lithium-ion batteries (LIBs) for large-scale electrical energy storage due to the abundance and low cost of sodium resources.[1–4] Unfortunately, graphite-based anodes, which are used in commercial LIBs, are unsuitable for SIBs because of the larger ionic radius of Na^+ (1.02 Å) and its higher ionization potential (−2.71 V *vs.* standard hydrogen electrode).[5,6] Consequently, developing suitable anode materials is a critical issue for advancing SIB technology.

[a]*Catalonia Institute for Energy Research – IREC, Sant Adrià de Besòs, Barcelona 08930, Spain. E-mail: acabot@irec.cat*
[b]*Universitat de Barcelona, Carrer de Martí i Franquès, Barcelona 08028, Spain*
[c]*Advanced Energy Storage Technology Research Center, Shenzhen Institute of Advanced Technology, Chinese Academy of Sciences, Shenzhen, 518055, China. E-mail: zhouxl@siat.ac.cn*
[d]*Synchrotron Light Research Institute (Public Organization), 111 University Avenue, Muang District, Nakhon Ratchasima 30000, Thailand*
[e]*ICREA Pg. Lluis Companys, 08010 Barcelona, Catalonia, Spain*

While alloy- and conversion-based anode materials show potential, they suffer from significant drawbacks, including high plateau voltage, poor cycling stability, and low initial coulombic efficiency (ICE).[7–9] Among alternative materials, hard carbon (HC) stands out due to its disordered, randomly graphitized structure, delivering a specific capacity of about 300 mAh g^{-1} and a low output voltage of around 0.2 V *vs.* Na^+/Na.[10,11] This notable performance, along with HC's excellent electrochemical stability and cost-effectiveness, makes it the most promising candidate for SIB anodes.

HCs typically consist of randomly stacked graphene layers with a highly disordered architecture, like fallen from a graphene-based house of cards.[12,13] HCs are also characterized by a high concentration of defects, heteroatoms, pores, and diverse surface functional groups, which contribute to their structural inhomogeneity and complexity.[14–16] This unique arrangement of highly defective graphite-like (C-sp^2) layers with large interlayer spacing provides numerous active sites and supports multiple Na^+ storage mechanisms, resulting in a high specific capacity.[17–19]

However, this complexity also presents challenges in understanding and optimizing HCs as SIB anode materials. The diverse range of Na^+ storage mechanisms, such as adsorption, intercalation, pore filling, and the related quasi-metallic sodium condensation, coupled with the structural and compositional variability among different HCs, has led to ongoing debate in the scientific community.[20,21] This controversy stems from the uncontrolled diversity in the architectures and compositions of HCs being studied, making it difficult to establish a clear relationship between structure, composition, and electrochemical performance.[22–24] Therefore, further research is needed to clarify how each of these factors influences Na^+ storage and to optimize HCs for better performance in SIBs.

To investigate Na^+ storage mechanisms in HC anodes, their performance across distinct voltage regions during the sodiation and desodiation processes needs to be analyzed. HC exhibits two characteristic regions: a sloping region above 0.1 V *vs.* Na^+/Na and a plateau region below 0.1 V *vs.* Na^+/Na. Current understanding identifies three primary mechanisms for Na^+ storage in HCs: (i) adsorption at surface/defect sites, (ii) intercalation/insertion of Na^+ between well-defined and relatively ordered graphite-like layers, and (iii) filling of interlayers and pores involving Na^+ ions occupying disordered and expanded graphene-like layers or voids within the carbon matrix.[17,25,26] Besides, a quasi-metallic sodium mechanism has been proposed recently, where Na^+ ions at a voltage close to 0 V *vs.* Na^+/Na form solid sodium in the nanopores, resulting in the large plateau region, particularly in the closed pore structure.[27–29] Most studies attribute the sloping region to Na^+ adsorption at defect sites and on disordered graphene-like sheets, while the plateau region, crucial for enhancing output voltage and energy density, remains controversial regarding whether intercalation, pore filling, adsorption, or nanocluster formation is the dominant mechanism.[14,15]

The electrochemical performance of Na^+ storage in HC anodes is influenced by several critical factors, including C-sp^2, porosity, pore size, surface area, defects, and heteroatom content. As a result, extensive research has focused on diverse features such as microstructure, heteroatom doping, and surface properties, uncovering multiple Na^+ storage mechanisms closely tied to the varied parameters.[17]

Strategies to improve the capacity of the plateau region have focused on controlling graphitization and pore structure. For example, increasing carbonization temperatures has been shown to enhance the plateau capacity by promoting graphitization and adjusting the size of closed pores. This has been linked to quasi-metallic sodium formation in micropores, which has been proposed as a key factor in boosting the plateau capacity. Studies by Choi *et al.*[30] and Zhang *et al.*[28,31,32] demonstrated that high carbonization temperatures could induce the formation of these nanoclusters, contributing to a larger plateau region and supporting the pore-filling mechanism.[33] Other researchers, such as Tang *et al.*[27] and Zheng *et al.*,[34] confirmed that closed micropores are crucial for sodium storage in the plateau region, providing sites for sodium nanocluster formation. Additionally, surface modifications and catalytic processes have been employed to enhance graphitization and reduce defect density, further improving Na^+ intercalation and storage performance.[14] Efforts have also been made to optimize micropore sizes to enhance Na^+ filling and intercalation, thereby increasing the plateau region and the overall HC capacities.[35,36]

However, these studies often deviate from the ideal 'house of cards' model for HC anodes, which envisions randomly stacked graphene layers and is essential for understanding key storage processes.[12,37,38] Additionally, despite significant advances, the debate remains vivid, highlighting the need for a clearer understanding of Na^+ storage mechanisms. This contrasts with graphite anodes in LIBs, where the ultra-low porosity and high crystallinity enable intercalation as the primary electrochemical storage mechanism. This well-established intercalation mechanism in LIB graphite anodes provides a valuable benchmark for understanding and optimizing other carbon-based anodes.[39,40] Thus, developing a precise and comprehensive structural model for HC anodes and establishing a clearer structure-performance relationship is critical to advancing our understanding of Na^+ storage mechanisms and optimizing these materials for SIBs.

Due to the complex structure of natural materials, achieving this requires the preparation of model HCs with well-controlled structures by carefully selecting the precursors and optimizing synthesis conditions, thereby the control variable method was difficult employed to elucidate the influence of individual factors on the sodium storage mechanism, such as pores, microstructure, morphology, defects, sp^2-C structure, and so forth on, leading to the complex sodium storage mechanisms. In this context, to explore the connection between pore structure and electrochemical behavior, it is essential to establish key characteristic behaviors, such as the intercalation/deintercalation mechanism in graphite for Li storage, which is referred to as the 'card of house model' in sodium storage.

N-doped HC serves as an ideal model due to its notable pseudocapacitive contribution in Na^+ storage, making it highly responsive to changes in both the slope and plateau regions.[41] Additionally, carbonization of polymers results in HC materials with fewer pores, avoiding the natural microstructures of biomass, closely resembling the ideal HC model.[41]

In this study, we present the synthesis of nitrogen (N) and oxygen (O) co-doped HC (NOC) nanosheets with ultra-low pore volume and specific surface area, achieved through a one-step amine-aldehyde condensation reaction. These NOC nanosheets serve as a model HC system featuring isolated, tightly packed graphene-like layers, in the absence of open pores, closely resembling a "house of cards" architecture. The incorporation of heteroatoms is intended to improve electrical conductivity, introduce structural defects, and provide active sites, thereby enhancing specific capacity.[41] Additionally, heteroatom doping of HC lowers resistance for alkaline metal ions and prevents quasi-metallic sodium condensation.[42] Overall, by investigating the sodium storage mechanism within the disordered carbon of this layered NOC 'house of cards' model, we aim to provide critical insights to enhance the understanding and optimization of SIBs.

2. Experimental section

2.1 Chemicals

Whatman glass fiber (Whatman, GF/A), *N*-methyl-2-pyrrolidone (NMP), sodium metal (Na, 99%), *p*-phenylenediamine ($C_6H_4(NH_2)_2$, 98%), and terephaladehyde ($C_6H_4(CHO)_2$, 97%), were purchased from Sigma-Aldrich. Mili-Q water (18 MΩ cm^{-1}) was supplied by a Purelab Flex from Elga. Ethanol was of analytical grade and obtained from Lestlab Delivering Solutions L.U. Commercial hard carbon (C-HC) was purchased from MTI (No. SIB-BHC300). Activated Carbon (AC) was purchased from KURARAY (YP80F) with a surface area of 2100 ± 200 m^2 g^{-1}. Copper foil (9 mm of thickness), carbon black (CB, Super C45), polyvinylidene fluoride (PVDF), 1.0 M sodium hexafluorophosphate in ethylene carbonate, and diethyl carbonate (1.0 $NaPF_6$ in EC–DEC (1 : 1, v/v)), 1.0 M sodium perchlorate in ethylene carbonate, and diethyl carbonate ($NaClO_4$ in EC–DEC (1 : 1, v/v)), and sodium trifluoromethanesulfonate in iethylene glycol dimethyl ether (1.0 M NaOtf in DIGLYME) were purchased from Guangdong Canrd Co. Ltd. All the chemicals were used as received, without further purification.

2.2 Synthesis NOC

Typically, terephaladehyde (170 mg) was added to 100 mL of deionized water and stirred vigorously for 30 min to obtain a homogeneous white suspension. Next, *p*-phenylenediamine (135 mg) was added to the suspension and continuous stirring for 4 h. The as-obtained suspension was centrifugated at 8000 rpm for 3 min and washed three times with ethanol and water. The as-obtained brown solids were pyrolyzed at 900 and 1000 °C for 4 h at the heating rate of 3 °C min^{-1} in the Ar atmosphere, and the products are annotated as NOC-9 and NOC-10, respectively.

2.3 Materials characterization

The morphology and elements information of NOC were checked by a field-emission scanning electron microscope (SEM) (HITACHI S-4800) and transmission electron microscopy using a JEOL JEM-3200FS, operating at 200 kV with a point-to-point resolution of 0.19 nm. A JEOL JEM-3200FS field emission TEM equipped with an Oxford Instruments EDS analyzer conducted the EDS of TEM. *In situ* XRD patterns were collected on a SmartLab (Rigaku, Japan) Diffractometer with Cu Kα radiation source (λ_1 = 1.540593 Å) over the 10–30° 2θ range. The Raman spectrum of samples was obtained on a Raman spectrometer (532 nm) (HORIBA XploRa PLUS) with a frequency range from 500 to 3500 cm^{-1}. The peak areas in the Raman spectra were calculated from the peak areas mediating proper correction according to the Origin 2021 software. The Brunauer–Emmett–Teller (BET) surface area analysis was conducted on the ASAP 2020HD88 instrument. Before the adsorption–desorption measurement, all the samples were heat-treated at 220 °C for 12 under vacuum to remove the moisture trapped in the microstructure. X-ray photoelectron spectroscopy (XPS) (ESCALAB 250Xi, Thermo Fisher) analyzed the elemental composition and chemical states. Binding energy values were corrected using the C 1s peak at 284.8 eV. The atomic fractions (%) were calculated from the peak areas mediating proper correction according to the Origin 2021 software. To avoid interference from gas adsorbed in carbon materials, all samples were dried at 110 °C in a vacuum oven for 12 hours and subjected to Ar etching for 5 seconds before the XPS test.

2.4 SAXS and WAXS characterization

The *d*-spacing of the crystal plane (002) was investigated using wide-angle X-ray scattering (WAXS). The experiments were measured using a multipole wiggler source on Beamline 1.3 W (BL1.3W: SAXS) of the Synchrotron Light Research Institute (SLRI, Public Organization, Thailand). A MarCCD Rayonix SX165 detector with a sample-to-detector distance of 800 mm for SAXS and 110 mm for WAXS was used and the samples were exposed to X-ray emission (λ = 1.38 Å) at room temperature for 5 min. The 2D SAXS and WAXS images were reduced and radially averaged by the program SAXSIT, developed by SLRI staff, to obtain 1D scattering curves. The modified Porod model, as described by Stevens and Dahn,[43] was used to fit the 1D scattering curves to identify nanopore diameter:

$$I(q) = \frac{A}{q^4} + \frac{Ba^4}{(1 + a^2q^2)^2} + C \quad (1)$$

where q is the wavevector, A and B are the combined total surface areas of the large and small pores, C represents the constant background term, and a is wavevector, is characteristic length over which electrodensity variations occur. The radius of gyration, R_g, defined by Porod as the mean square distance from the center of gravity of the scattering object (*i.e.*

the nanopore),[44] is related to a by $R_g = a\sqrt{6}$, and provides a measure of the size of the nanopres. The radius of gyration of a sphere of radius R is $R_g^{\text{sphere}} = R\sqrt{0.6}$. Therefore, the radius of a spherical pore is equivalent to the Debye's length,[45] over which the scattering power varies and which is related to average pore size, noted as the radius of a spherical closed pore by:

$$R = a\sqrt{10} \quad (2)$$

2.5 NEXAFS measurement

NEXAFS was performed at the BL3.2Ub of the Synchrotron Light Research Institute (SLRI) (Public Organization), Nakhon Ratchasima, Thailand. The beamline photon source covers an energy range of 40 to 1040 eV at the resolving power of 10 000. The synchrotron radiation source at the storage ring was generated using a beam energy of 1.2 GeV. The NEXAFS spectra were measured in the PEY mode and the light polarization was parallel to the surface at any incident light angle. The intensity of the incident photon beam (I_0) was monitored at a gold mesh in front of the samples, enabling the PEY signal to be normalized by I_0. The total energy resolution was approximately 0.5 eV. Absolute photon energy was obtained by aligning the π^* (C=C) peak position of graphite to the literature.[46] Uncertainty in the calibrated wavelength was estimated to be ±0.2 eV. The carbon K-edge NEXAFS spectra were measured in the energy range of 275 to 335 eV at an energy step of 0.1 eV.

2.6 Electrochemical measurements

Electrochemical tests of the batteries were performed on CR2032-type coin cells. The NOC electrode was prepared by spreading a slurry of 80 wt% active material, 10 wt% carbon black, and 10 wt% PVDF binder in NMP on a copper foil, drying at 110 °C overnight in a vacuum oven. Subsequently, the anode electrode was cut to a diameter of 10 mm. The loading mass of active materials was kept constant at around 1.5 mg cm^{-2}. The half-cell was composed of sodium foil and was punched into 12 mm circular foil as an anode electrode, the NOC electrode as the cathode side, and the glass fiber with a diameter of 16 mm was used as a separator. The Na-DIB comprised the NOC as an anode electrode, a graphite foil with a 12 mm diameter, and a glass fiber with a 16 mm diameter as the separator. 1.0 M $NaPF_6$ was added in EC–DEC (1 : 1, v/v) as electrolytes in half-cell and 60 μm electrolyte per cell. The coin cells were assembled in the glovebox and measured at room temperature. Before cycling, all coin cells were aged for 4 h to ensure sufficient electrolyte penetration. Galvanostatic charge/discharge tests were carried out on the Neware BES-4008 battery test system with a potential range set between 0.01 and 2.0 V (*vs.* Na^+/Na). Cyclic voltammetry (CV) tests were performed on a BCS-810 battery tester from Bio-Logic at different scan rates with a potential range set from 0.01 to 2.0 V (*vs.* Na^+/Na). Electrochemical impedance spectroscopy (EIS) measurements were carried out using a sinusoidal voltage with an amplitude of 10 mV and a frequency from 10 kHz to 0.01 Hz.

The sodium quasi-metallic test. The hard carbon electrode was prepared in a fully discharged state (0.01 V *vs.* Na^+/Na) in half-cell at a current of 50 mA g^{-1}, removed from the coin cell at the Ar glovebox, and sealed into the glass bottle. Then, a needle was used to inject 10 mL of the 1% phenolphthalein in anhydrous ethanol into the glass bottle at the glovebox, keeping the 5 min, and the color change was observed.

2.7 Galvanostatic intermittent titration technique (GITT)

GITT was applied at a current of 0.2 C for 10 min, accompanied by a 20 min rest interval to calculate the diffusion coefficient of sodium ions (D_{Na^+}).

$$D_{Na^+} = \frac{4}{\pi\tau}\left(\frac{m_B V_M}{M_B S}\right)^2 \left(\frac{\Delta E_s}{\Delta E_t}\right)^2 \quad (3)$$

where m_B represents the mass of active material of sodium ion inserted/ex-insert the electrode during a single current pulse, τ represents the pulse duration, S represents the active surface area, V_M and M_B represent the molar volume of carbon and molecular mass of sodium, and ΔE_s and ΔE_t represent the voltage changes caused by pulse relaxation time and galvanostatic current, respectively. ΔE_s and ΔE_t values were obtained from the GITT curve.[47]

3. Results and discussion

Compared to biomass-derived precursors, polymers offer a simpler structure and better control over micro-/mesostructure during carbonization. Therefore, model HC samples with low porosity were produced through the carbonization of polymers containing linear chains of polyphenylene rings, which are known for their ability to carbonize into graphene-like carbon with low porosity. Specifically, to prepare NOC nanosheets, an amine-aldehyde resin was synthesized in an aqueous solvent (Fig. S1, see details in the SI).[48] Fourier-transform infrared (FTIR) spectra of the precursor polymer confirmed the successful polymerization reaction. The transmittance band at 1608 cm^{-1} corresponds to the vibration of the imine bond group (–N=C–), while the characteristic band at 850 cm^{-1} indicates the presence of 1,4-substituted benzene rings (Fig. S2).

NOC samples, named NOC-9 and NOC-10, were then prepared by thermally annealing the amine-aldehyde resin at 900 and 1000 °C, respectively. Scanning electron microscopy (SEM) (Fig. S3) revealed that both samples consist of nanosheet aggregates. Transmission electron microscopy (TEM) images (Fig. 1a, b, S4a and b) showed multi-layer graphene-like carbon nanosheet stacking, with an amorphous structure. High-resolution TEM (HRTEM) analyses (Fig. 1c) further demonstrated that the nanosheets contained randomly oriented short-range order graphitic domains, with d_{002} interlayer spacings of 4.0 Å for NOC-9 and 3.9 Å for NOC-10 (Fig. 1c and S4c). The interlayer spacings for both samples are larger than that of graphite (3.4 Å) and are at the limit of the spacing typically required to facilitate efficient Na^+ diffusion in disordered

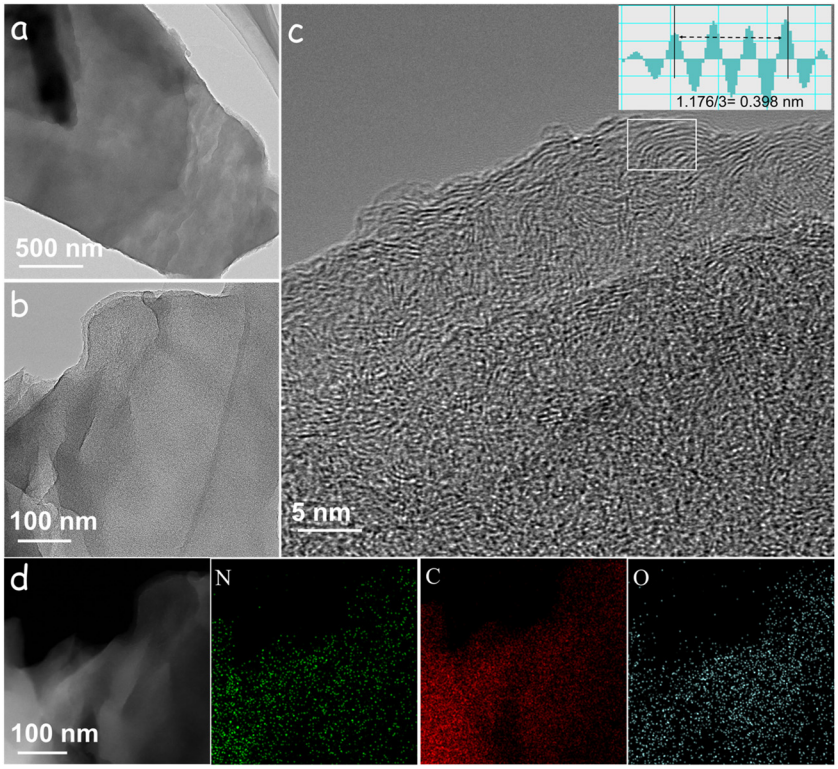

Fig. 1 Electron microscopy characterization of NOC-10. (a and b) TEM images. (c) HRTEM image showing interlayer spacing (inset). (d) EDS elemental maps of a nanosheet.

graphene-like structures and enable Na^+ filling/intercalation in HC (>4.0 Å).[1] NOC samples showed a very low porosity, with NOC-9 exhibiting some closed pores, visible as white rings in the HRTEM images. Energy dispersive X-ray spectroscopy (EDS) compositional maps (Fig. 1d) confirmed the homogeneous distribution of C, N, and O atoms across the nanosheets.

Wide-angle X-ray scatting (WAXS) patterns, obtained with a synchrotron X-ray source at room temperature, display two peaks corresponding to the (002) and (100) graphitic crystal planes (Fig. 2a). According to Bragg's Law, the (002) peak located at the 2θ = 19.57° and 20.19°, for NOC-9 and NOC-10, reveal interlayer spacings 4.06 and 3.94 Å, respectively, which are consistent with HRTEM data.

Small-angle X-ray scattering (SAXS) was used to analyze the pore structure in the 1–100 nm range, independently of their open or close characteristics (Fig. S5). The SAXS scattering intensity, which is related to the porosity of HC,[43] indicates NOC-9 to exhibit a higher concentration of micropore/mesopore than NOC-10.[49] In contrast, NOC-9 exhibited some concentration of nano- and micropores in this region. By fitting the SAXS pattern using the Porod equation (Fig. 2b and c, fitting parameters are shown in Table S1), the a_1 values were directly related to the pore structures in NOC-9 and NOC-10, which were fitted to be 0.20837 and 0.046564, respectively.[50] These results revealed the presence of abundant pore structure of NOC-9, calculating to the average pore diameter is 1.3 nm, whereas NOC-10, not only displayed a lower surface area but also a negligible pore structure.

Both samples display type II N_2 adsorption–desorption isotherms with relatively low surface areas of 9.6 and 7.6 $m^2\ g^{-1}$, for NOC-9 and NOC-10, respectively (Fig. S6a). These values are similar to those of a reference commercial HC (C-HC purchased from MTI) at 8.0 $m^2\ g^{-1}$.[51] Besides, both samples show a low pore volume (Fig. S6b), particularly NOC-10. It is important to note that N_2 adsorption/desorption measurements only capture the open surface porosity and pore sizes larger than 0.7 nm, corresponding to the size of the probing N_2 molecule.[52] Combining the SAXS and BET results, it is concluded that the two NOCs but particularly NOC-10 exhibit low pore structure and surface areas, with NOC-10 notably demonstrating a pore-free configuration. In contrast, NOC-9 is similarly unlikely to exhibit a closed-pore structure due to its low open surface area, akin to that of NOC-10.

Near-edge X-ray absorption fine-structure (NEXAFS) analyses were used to gain additional insight into the C, N, and O chemical states within NOCs. The C K-edge NEXAFS spectra of carbon materials at the negative bias voltage of 0.0 and 0.5 kV are shown in Fig. 2d and S8. All the spectra are decomposed into two-edge structures. A pre-edge resonance at 285 eV is assigned to the transition from the C 1s orbital to the unoccupied π^* orbitals principally originating from sp^2 sites (C=C), including the contribution of the sp sites (C≡C) if present.[53] The broadband between an energy edge from 288 to 320 eV is

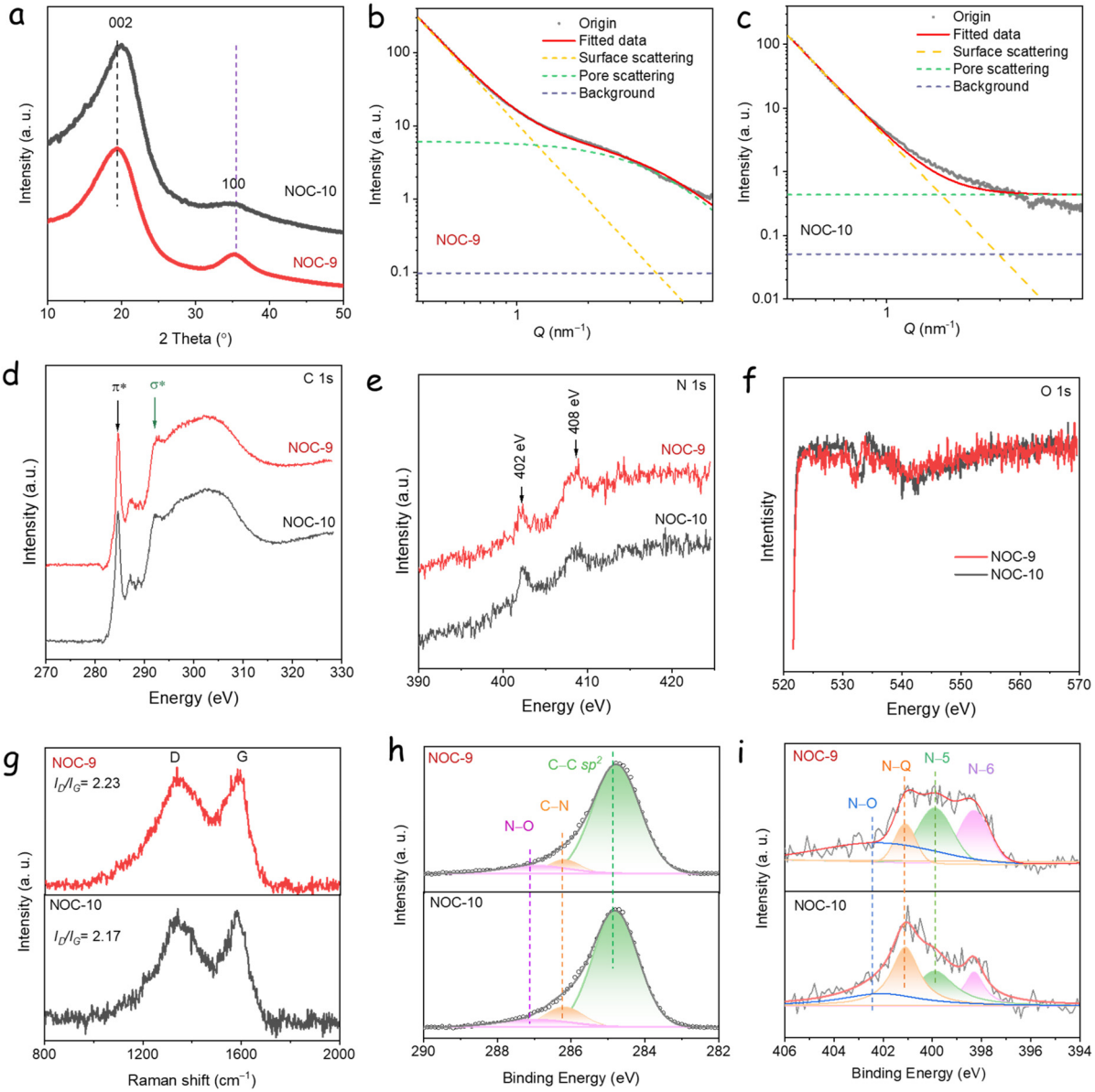

Fig. 2 Physical properties of NOC. (a) WXAS patterns and amplification of the (002) peak in NOC samples. (b and c) Fitted SXAS patterns for NOC-9 (b) and NOC-10 (c). (d–f) C K-edge (d), N K-edge (e), and O K-edge (f) NEXAFS spectra. (g) Raman spectra. (h and i) XPS spectra of C element (h) and N element.

related to the C 1s → σ* transitions at the sp, sp^2, and sp^3 sites in the amorphous carbon materials, particularly the peak positioned between 290 and 295 eV originates from the σ* bonding structure.[54,55] The spectrum was decomposed into several Gaussian peaks (Fig. S7), and the areas of $sp^2/(sp + sp^2 + sp^3)$ are 64% and 67% for NOC-9 and NOC-10, respectively. Due to the high carbonization temperature, NOC-10 exhibits a higher sp^2 contribution assigned to the graphitization structure. Fig. 2e shows the N K-edge NEXAFS spectra for N 1s in NOC. This clearly shows the two peaks at around 402 and 408 eV, which are attributed to pyridinic N (N-6) and pyrrolic N (N-5), respectively.[56,57] This implies that NOC-9 has a higher content of N-5. The O K-edge NEXAFS displays a peak at around 537 eV, assigned to the C–O bonding (Fig. 2f).[58] O atoms mainly exist at the edges of carbon materials and are rarely present within carbon materials.

The Raman spectra of the two samples exhibit characteristic G and D bands at 1590 and 1350 cm^{-1}, respectively. These bands correspond to graphitic carbon (in-plane stretching vibration of sp^2 carbon atom in rings and chains) and defects in sp^2 carbon structure (Fig. 2g).[59] The integral intensity ratios I_D/I_G provide insights into the degree of defects in sp^2 carbon, described as the 2.23 (NOC-9) and 2.17 (NOC-10).[60,61] Based on the $sp^2/(sp + sp^2 + sp^3)$ results, the semi-quantitative defect levels are 1.42 for NOC-9, and 1.45 for NOC-10, respectively. Therefore, the NOC-10 has a higher defect concentration than NOC-9.

X-ray photoelectron spectroscopy (XPS) analysis confirmed the presence of N, O, and C (Fig. S9). The high-resolution C 1s XPS spectrum (Fig. 2h) revealed the presence of carbon within three different chemical environments, sp^2-hybridized (C-sp^2, 284.8 eV), bond with nitrogen (C–N, 286.2 eV), and bond with oxygen (C–O, 287.2 eV).[62] The N 1s XPS spectrum (Fig. 2i) shows the presence of pyridinic N (N-6, 398.3 eV), pyrrolic N (N-5, 399.9 eV), quaternary N (N-Q, 401.1 eV), and pyridinic-N–O (N–O 402.1 eV).[63] The contribution of each component and the ratio of N and C are displayed in Table S2, showing that the pyridinic and pyrrolic N decrease with the carbonization temperature, while the quaternary N increases. Overall, both NOC samples exhibit similar C, O, and N chemical states.

The SIB electrochemical performance of NOC samples was evaluated in a half-cell configuration using 2032-type coin cells, operating within a voltage window of 0.01 to 2.0 V *vs.* Na^+/Na. The electrolyte used was 1.0 M $NaPF_6$ in a mixture of ethylene carbonate (EC) and diethyl carbonate (DEC) in a 1 : 1 volume ratio. Fig. 3a shows the 3rd cyclic voltammetry (CV) cycle recorded at a scan rate of 0.1 mV s^{-1}. For both samples, an anodic peak is observed at around 0.15–0.16 V, which corresponds to the sodiation process in the plateau region, typically associated with Na^+ insertion.[17] NOC-9 displays prominent peaks at approximately 0.67 V during both the oxidation and reduction processes, and these peaks are almost symmetrical, indicative of pseudocapacitive behavior occurring in the slope region.[64,65] As expected, NOC-10, which has a lower surface area and fewer nanopores, exhibits a more pronounced redox reaction at the plateau region and reduced redox activity in the slope region.

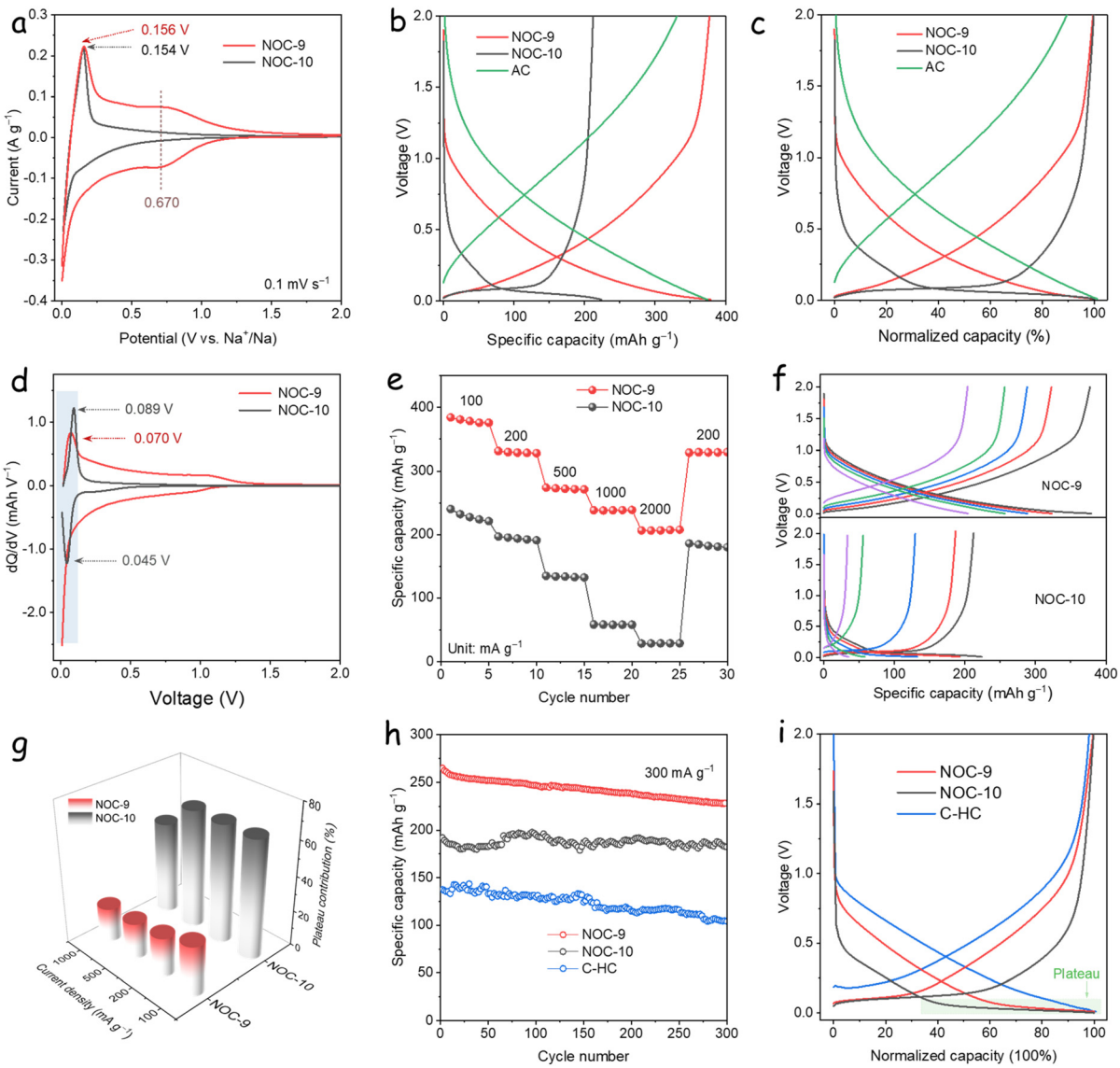

Fig. 3 Electrochemical performance. (a) CV curves at 0.1 mV s^{-1}. (b) GCD curves at 100 A g^{-1}. (c) Normalized capacity. (d) Corresponding d*Q*/d*V* curves. (e) Rate tests in the range of 100 to 1000 A g^{-1}. (f) GCD profiles at current densities of 100–1000 mA g^{-1}. (g) Corresponding plateau contribution to the discharge capacity. (h) Cycling stability. (i) GCD curves after 300th cycles.

As shown in the galvanostatic charge–discharge (GCD) curves (Fig. 3b), the NOC-9 and NOC-10 electrodes deliver reversible capacities of 380 and 215 mAh g^{-1} at a current density of 100 mA g^{-1}, respectively. Interestingly, NOC-10 exhibits typical Na^+ storage electrochemical behavior of HC materials, characterized by a large plateau region below 0.1 V and a smaller slope region above 0.1 V. In contrast, NOC-9 displays the characteristic Na^+ storage behavior of N-doped HC, with a larger slope region, reflecting its distinct capacitive contribution.[41,66] As the supplement sample, activated carbon (AC) with a large surface area application on the supercapacitor exhibits similar curves to NOC-9 in the sodiation process, and no plateau is observed during the charging process, presenting the capacitance behavior for sodium storage.

To better compare the performance of the two NOC samples, the GCD curves are normalized and plotted against capacity in Fig. 3c. In NOC-10, the plateau region contributes 68% of the total discharge capacity, corresponding to 146.2 mAh g^{-1}. In contrast, NOC-9 exhibits a plateau contribution of only 30%, equivalent to 114.0 mAh g^{-1}. Consequently, the primary capacity contribution in NOC-10 occurs below 0.5 V *vs.* Na^+/Na, with just 8% of the capacity originating from above 0.5 V during the sodiation process.[41] This low-voltage slope region behavior is rarely observed in heteroatom-doped HC materials.[41,67] Additionally, NOC-10 exhibited a significantly higher ICE of 58.3%, compared to 40.7% for NOC-9 (Fig. S10).

Fig. 3d presents the differential capacity (dQ/dV) curves, which help distinguish the redox reactions occurring in the plateau region during the GCD tests. The two electrodes exhibit distinct electrochemical behavior below 0.5 V: NOC-10 shows well-defined peaks at 0.045 and 0.089 V, indicating complete redox processes within the plateau. In contrast, the NOC-9 electrode exhibits an incomplete peak in the plateau region, with the oxidation peak located at a voltage below 0.01 V *vs.* Na^+/Na. Thus the redox reaction in NOC-9 is occurring at a lower voltage. Additionally, GCD curves at 100 mA g^{-1} were recorded in the voltage range of −0.1 to 2.0 V to simulate the Na^+ deposition behavior (quasi-metallic sodium), showing a significant plateau region accounting for 54% of the capacity (Fig. S11a). The corresponding dQ/dV curves for NOC-9 (Fig. S11b) reveal that the complete peak in the plateau region is located at −0.0049 V *vs.* Na^+/Na, below the sodium deposition potential, possibly attributed to the Na^+ deposition potential. This suggests that quasi-metallic sodium may form during the sodiation process in NOC-9, which could be advantageous for enhancing storage capacity through the filling mechanism. We attribute this behavior to the specific micropore structure and heteroatom doping present in NOC-9, which likely facilitates the formation of these sodium nanoclusters, as has been observed in previous studies.[35]

To illustrate the universality of the sodium storage behavior of NOCs, two conventional electrolytes were additionally employed as supplementary experiments: 1.0 M $NaClO_4$ in EC : DEC (1 : 1 v/v) and 10 M NaOTf in DIGYDME. As demonstrated in Fig. S12, NOC-9 exhibits a smaller plateau region across different electrolytes, whereas NOC-10 displays a larger plateau and a pronounced oxidation peak. These results indicate that the NOCs exhibit distinctly different plateau and slope regions in these electrolytes, thereby demonstrating their universality.

Fig. 3e and f compare the rate performance of the NOC electrodes. NOC-9 shows significantly higher capacities across the current range of 100–1000 mA g^{-1} compared to NOC-10. The GCD profiles of both electrodes exhibit well-defined plateaus. As depicted in Fig. 3g, NOC-9 delivers reversible capacities of 145, 71, 57, and 48 mAh g^{-1} in the plateau region at current densities of 100, 200, 500, and 1000 mA g^{-1}, respectively. In comparison, NOC-10 shows capacities of 150, 129, 89, and 41 mAh g^{-1} at the same current densities. Although NOC-9 has a higher overall discharge capacity, NOC-10 demonstrates higher capacities in the plateau region.

To further illustrate the electrochemical properties of NOC electrodes, Fig. 3h compares the cyclic stabilities of the NOC-9, NOC-10, and C-HC electrodes at a current density of 300 mA g^{-1} (equivalent to about 2.55 C in a full-cell based on HC||$Na_3V_2(PO_4)_3$). NOC-9 shows the highest reversible capacity throughout the cycling process, indicating strong overall performance. However, NOC-10 exhibits the highest capacity retention, demonstrating superior stability over extended cycles. To clearly distinguish the behavior of the plateau region after prolonged cycling, the GCD potentials are plotted against normalized capacity in Fig. 3i and S13. Under a current of 100 mA g^{-1}, the C-HC exhibits a specific capacity of 321 mAh g^{-1} with a clearly plateau region. Furthermore, the normalized capacities are comparable to those of NOC-10 within the plateau region, implying the possibility of a filling mechanism existing. After 300 cycles at 300 mA g^{-1}, the reversible capacities are 228.5, 181.5, and 144.8 mAh g^{-1} for NOC-9, NOC-10, and C-HC samples, respectively. Thus, NOC-10 shows excellent retention in the plateau region during cycling, highlighting its superior performance in retaining plateau-region capacity compared to both NOC-9 and C-HC. The stronger plateau retention of NOC-10 is likely due to its more stable microstructure, which reduces capacity fade and enhances long-term electrochemical stability.

Overall, the above results reveal that a carbonization temperature difference of only 100 °C during the synthesis process leads to a significant difference in the Na^+ storage electrochemical behavior, even though both samples are derived from the same precursor. The NOC-10 electrode behaves similarly to the reference C-HC, with a pronounced plateau region below 0.1 V, whereas NOC-9 exhibits the typical Na^+ storage behavior of N-doped HC, characterized by a large slope region related to ion adsorption and pseudocapacitance. According to previous studies, the heteroatom content in both NOC-9 and NOC-10 is expected to contribute to a considerable pseudocapacitive capacity, enhancing Na^+/Li^+ ion adsorption at defect sites, promoting additional active sites for ion storage, and thus presenting the significant slope plateau at >0.1 V.[68] Based on these results, we discuss below the notable differences in

electrochemical behavior for sodium storage exhibited by the NOC-10.

Ex situ Raman spectroscopy and *in situ* XRD analyses were employed to gain further insight into the Na^+ intercalation mechanism in NOC-10 at 50 mA g^{-1}. Generally, when electrons transfer to the graphite-like layers along with Na^+ ions, the occupation of the conjugated graphite-like structure leads to the formation of an antibonding band, which lengthens and weakens the C–C bonds. This effect is observed as a red-shift of the G-band in the Raman spectra.[34,69] On the other hand, the adsorption of Na^+ ions at defective sites and within pores restricts the breathing vibration of C-sp^2 rings at defect and edge sites of the carbon layer, causing a weakening of the D-band.[70,71] The *ex situ* Raman spectra recorded at different voltage states during the sodiation and desodiation process over 5 cycles at 50 mA g^{-1} are shown in Fig. 4a. During sodiation, the G-band peak is slightly red-shifted and weakened at 0.05 V and 0.01 V (corresponding to the plateau region), consistently with Na^+ ions intercalating into the graphite-like interlayers. During the desodiation process, the G-band shows minimal change initially but then returns to its original position, indicating a reversible structural modification in NOC-10. Interestingly, the relative D-band intensity increases during the plateau region, suggesting that the HC structure retains a higher degree of defects during this process. In contrast to previous works showing I_D/I_G to decrease and recover during sodiation and desodiation (Fig. 4b), the I_D/I_G of NOC-10 increases (1.99 to 3.17) in the sodiation and recovers in the desodiation process, whereby the NOC-10 electrode kept the high intensity of the D-band (defects in sp^2 carbon). As no weakening of the D-band is observed, we conclude that Na^+ ions do not undergo significant adsorption at defective sites or within pores in the slope region. In contrast, the I_D/I_G of NOC-9 decreases (2.14 to 1.11) with the Na^+ insertion, which is associated with the typical electrochemical behaviors in HCs, involving adsorption at defective sites or within pores (Fig. S14).

According to theoretical calculations, Na^+ ions have negative binding energies in planar graphitic layers with interlayer distances between 4.5 and 5.4 Å.[35] When Na^+ ions intercalate into graphite-like structures, the interlayer distance (d_{002}) is expected to increase. The *in situ* XRD patterns of NOC-10, focusing on the (002) peak, were recorded during the initial cycles at 50 mA g^{-1} (Fig. 4c). Notably, the intensity of the (002) peak remained unchanged throughout the sodiation and desodiation processes, indicating that little to almost no Na^+ ions intercalated into the graphite-like structures and negligible NaC_x compounds were formed, thus the volume of NOC-10 experienced minimal or no expansion.[31] Further analysis was conducted using high-precision SXRD (λ = 0.826) to examine the NOC electrodes in their fully charged/discharged state, as depicted in Fig. 4d. The SXRD spectrum of NOC-10 exhibits virtually no distinct peaks, whereas NOC-9 displays a broad peak at 2θ = 18.2°, corresponding to the orthogonal system of Na metal in the fully discharged state.[72] Upon full charging, the patterns revert to their previous state, indicating the presence of reversible sodium nanoclusters in NOC-9, and the (002) peak right-shifts, indicating that the Na^+ de-intercalation occurs in the graphite-like structure. In contrast, NOC-10 displays a (002) peak with the same position, indicating that NOC-10 exhibits less intercalation behavior. Combining the G-band shifts observed in the *ex situ* Raman spectra with *in situ* XRD results, we conclude that there is a minor effect of the Na^+ insertion on the graphite-like structure of NOC-10, leading to a weakening of the G-band without modifying the (002) XRD peak. However, in NOC-10, the D-band intensity and I_D/I_G ratio remain high across both the slope and plateau regions, suggesting that these defect sites do not significantly adsorb Na^+ ions. This observation implies that the defects are partially or fully inactive in the NOC-10 electrode, contrasting with previous reports and indicating a distinct Na^+ storage mechanism in this material.[1]

Given the similar adsorption and filling behaviors of alkali metal ions such as Na^+ and Li^+, the electrochemical performance of NOC electrodes in the slope region was further examined using lithium-based half-cells.[17,63] As shown in Fig. S15a, both NOC-9 and NOC-10 electrodes display smooth charge–discharge profiles within the voltage range of 0.1 to 1.0 V at a current density of 100 mA g^{-1}. The discharge capacities at the 2nd cycle were 669.0 mAh g^{-1} for NOC-9 and 579.8 mAh g^{-1} for NOC-10. The dQ/dV curves (Fig. S15b) exhibit a subtle and flat reduction peak around 1.0 V *vs.* Li^+/Li, suggesting that NOCs demonstrate typical HC electrochemical behavior for lithium storage, which contrasts with their behavior in sodium storage.[30]

To further investigate the Na^+ storage mechanism in NOCs, CV curves were recorded at scan rates ranging from 0.1 to 1.2 mV s^{-1} (Fig. S16). According to the Randles–Sevcik equation, the response current is divided into capacitive and diffusion contributions.[73] The capacitive contribution increases with increasing scan rate, while the diffusion coefficient in the carbon material limits the diffusive contribution. Thus, the NOC-10 exhibits a similar peak current in different scan rates, indicating that the diffusion behavior is dominant and there is little adsorption contribution, which is different from the NOC-9 electrode.

To investigate the presence of quasi-metallic sodium within the carbon materials, we immersed the fully sodiated electrode into a 1% phenolphthalein solution prepared in anhydrous ethanol and monitored the resulting color change (see details in the SI). Fig. 4e illustrates the results for the three HC samples. The C-HC sample displayed a purplish-red color, confirming the presence of quasi-metallic sodium. In contrast, NOC-9 and NOC-10 remained nearly colorless, indicating either a negligible amount or the absence of quasi-metallic sodium in these samples, even at the fully sodiated state.

To compare the kinetic properties of the two NOC electrodes, the galvanostatic intermittent titration technique (GITT) was employed to assess the apparent diffusion coefficient of Na^+ ions (D_{Na^+}) during the discharge process (Fig. 4f and g). As expected, the diffusion behavior in NOC-10 translated into a low voltage drop during the sodiation process, whereas the NOC-9 showed a higher voltage drop likely attributed to the

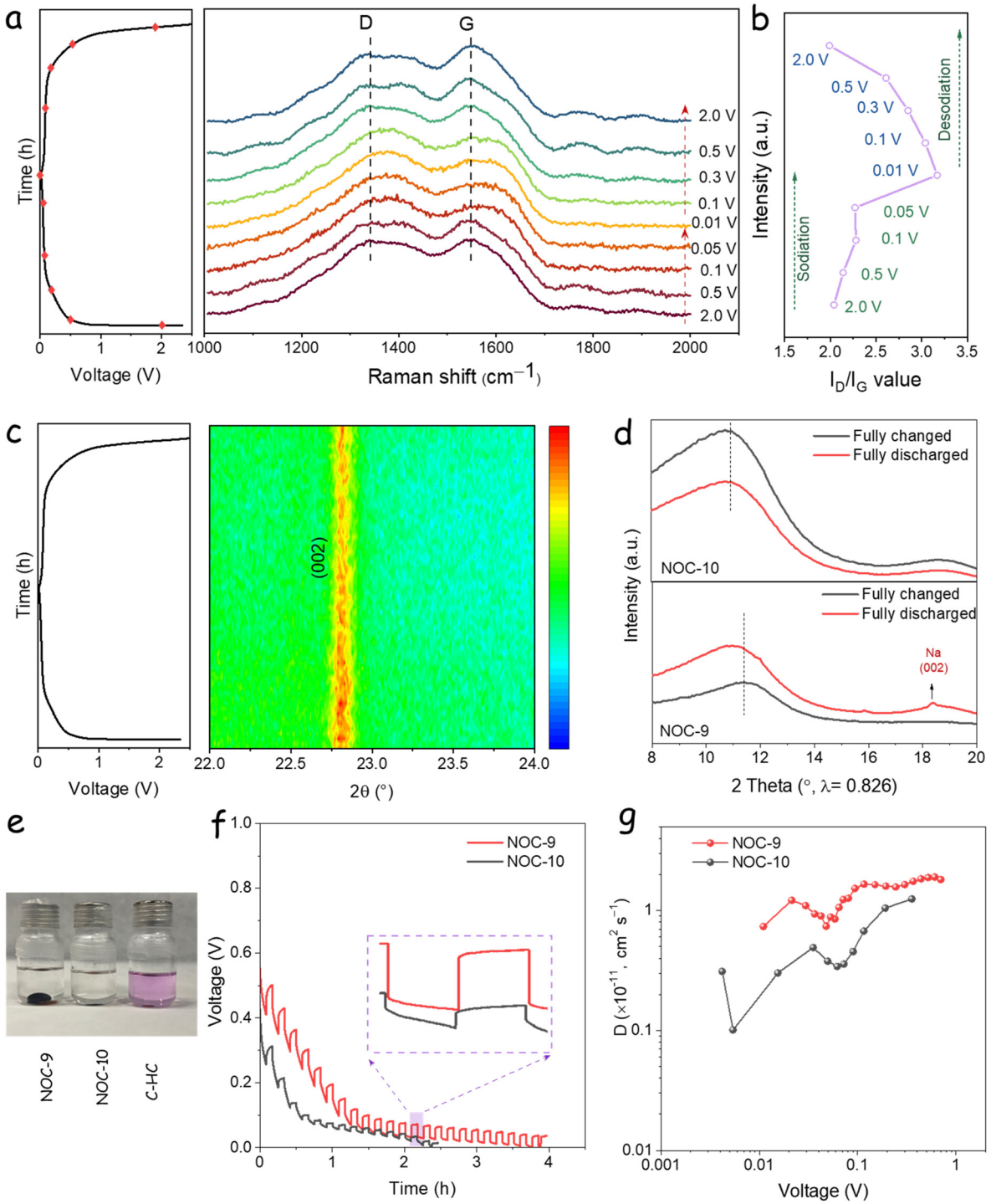

Fig. 4 Mechanistic study of the Na^+ storage process. (a) *Ex situ* Raman spectra from NOC-10 at 50 mA g^{-1}, corresponding to (b) I_D/I_G ratios. (c) *In situ* XRD patterns of NOC-10 at 50 mA g^{-1}. (d) The SXRD patterns of NOCs were out with the fully changed and fully discharged states. (e) Optical photograph of samples discharged to 0.01 V *vs.* Na^+/Na soaked in a 1% phenolphthalein ethanol solution for 5 min. (f) GITT curves at 300 mA g^{-1}. (g) Na^+ ions diffusion coefficient calculated from GITT.

pseudocapacitance contribution to the capacity. For both samples, D_{Na^+} increases progressively with sodiation and remains in the range of 0.1 to 5 × 10^{-11} cm^2 s^{-1} after 50 cycles (300 mA g^{-1}, 10-minute relaxation time), highlighting the rapid diffusion kinetics of Na^+ ions in these materials, meanwhile, which implies that different mechanisms exist in NOCs.

According to previous reports, nitrogen doping increases defect sites, which effectively enhances the specific capacity,

particularly the slope capacity. In this context, considering the distinct structural characteristics of NOC-10, featuring a nanopore-free, ultra-low surface area with tightly disordered carbon layers, and NOC-9, which contains some nanopores, the findings can be summarized as follows: (i) the increasing D-band intensity and I_D/I_G ratio during sodiation indicate that tightly stacked disordered graphene-like layers do not contribute to defect-adsorption responsible for the slope and plateau regions. Instead, only the nanopores introduce defect sites for Na^+ adsorption, highlighting that the contribution of defect-adsorption is highly dependent on the microstructure. (ii) The plateau region can be effectively enhanced by the presence of tightly stacked graphene-like layers in nanopore-free HC through the layer-filling mechanism.[74]

Building on these findings, we propose that the dominant Na^+ storage mechanism contributing to the plateau region in NOC-10 is the filling of tightly stacked disordered graphene-like layers, closely resembling the ideal "house of cards" model. This mechanism, referred to as the layer-filling mechanism, involves Na^+ ions occupying the interlayer spaces within disordered graphene-like structures, an intrinsic feature of HC materials. This concept can be extended to a broader range of HC materials comprising both tightly and loosely disordered carbon layers. Consequently, we propose the plateau capacity is primarily governed by the intrinsic microstructure of the carbon rather than by increasing surface area or introducing nanopores, strategies that are more effective for enhancing slope-region capacity. Moreover, this mechanism offers an explanation for why HCs carbonized at higher temperatures (including commercial HCs processed above 1300 °C) exhibit greater plateau capacities. Elevated carbonization temperatures promote the formation of tightly stacked disordered carbon layers while suppressing defect adsorption in the slope region, underscoring the critical role of structural disorder in optimizing Na^+ storage efficiency.[75]

4. Conclusion

In this study, we investigated the sodium storage mechanism in a carbon system that follows the "house of cards" model. By varying the polymer carbonization temperature, we synthesized model HCs to explore the influence of structural characteristics, chemical states, and electrochemical behavior on Na^+ storage capacity. Our analysis, combining *ex situ* Raman spectroscopy and *in situ* XRD, revealed that the slope/plateau-region capacity is mostly independent of nanopores or surface area, instead relying on intrinsic micro- and meso-structural features, through a layer-filling mechanism. This finding underscores that simply increasing surface area or introducing nanopores does not significantly enhance plateau-region capacity through this mechanism. Instead, optimizing precursor materials and carbonization methods emerges as a more effective strategy. This approach, together with tailoring the structure to enable the reversible formation of quasi-metallic sodium within pore structures, presents a promising avenue for further improving plateau-region capacity. Our insights provide a foundation for the design of high-performance carbon materials by focusing on key structural and processing factors, contributing to advancements in sodium-ion battery technology.

Author contributions

X. C. designed the experiments, investigated, and performed the formal analysis. N. K., P. B., and S. T. supported the NEXAS and SXAS measurements. X. L. conducted the Raman analysis and edited the manuscript. X. Z. and A. C. co-wrote the manuscript. X. Z. administered the project, resources, and funding.

Conflicts of interest

There are no conflicts to declare.

Data availability

The data supporting this article, including SEM images, XRD spectra, XPS spectra, and electrochemical measurements, have been included as part of the manuscript and supplementary information (SI). See DOI: https://doi.org/10.1039/d5eb00168d.

Additional data or materials used in this study are available from the corresponding author upon reasonable request.

Acknowledgements

This work was financed by European Excellent Science – Further and Emerging Technologies, National Natural Science Foundation of China (52272054), Natural Science Foundation of Guangdong Province (2024A1515011670), Shenzhen Science and Technology Planning Project (GJHZ20220913142809019). The authors gladly thank the Synchrotron Light Research Institute (SLRI) provided the synchrotron X-ray tests and analytical discussions. Part of the present work has been performed in the framework of the Universitat de Barcelona electrochemistry Ph.D program.

References

1 Y. Chu, J. Zhang, Y. Zhang, Q. Li, Y. Jia, X. Dong, J. Xiao, Y. Tao and Q. H. Yang, *Adv. Mater.*, 2023, 2212186.
2 X. Xiang, K. Zhang and J. Chen, *Adv. Mater.*, 2015, **27**, 5343–5364.
3 C. Vaalma, D. Buchholz, M. Weil and S. Passerini, *Nat. Rev. Mater.*, 2018, **3**, 1–11.
4 Y.-X. Yao, L. Xu, C. Yan and Q. Zhang, *EES Batteries*, 2025, **1**, 9–22.
5 P. K. Nayak, L. Yang, W. Brehm and P. Adelhelm, *Angew. Chem., Int. Ed.*, 2018, **57**, 102–120.

6 J.-Y. Hwang, S.-T. Myung and Y.-K. Sun, *Chem. Soc. Rev.*, 2017, **46**, 3529–3614.
7 L. Li, Y. Zheng, S. Zhang, J. Yang, Z. Shao and Z. Guo, *Energy Environ. Sci.*, 2018, **11**, 2310–2340.
8 M. D. Slater, D. Kim, E. Lee and C. S. Johnson, *Adv. Funct. Mater.*, 2013, **23**, 947–958.
9 C. Wu, Y. Yang, Y. Zhang, H. Xu, W. Huang, X. He, Q. Chen, H. Dong, L. Li and X. Wu, *Angew. Chem., Int. Ed.*, 2024, **63**, e202406889.
10 H. Hou, X. Qiu, W. Wei, Y. Zhang and X. Ji, *Adv. Energy Mater.*, 2017, **7**, 1602898.
11 C. Wu, Y. Yang, Y. Zhang, H. Xu, X. He, X. Wu and S. Chou, *Chem. Sci.*, 2024, **15**, 6244–6268.
12 D. A. Stevens and J. R. Dahn, *J. Electrochem. Soc.*, 2000, **147**, 1271–1273.
13 Y. Liu, J. Xue, T. Zheng and J. Dahn, *Carbon*, 1996, **34**, 193–200.
14 H. Au, H. Alptekin, A. C. Jensen, E. Olsson, C. A. O'Keefe, T. Smith, M. Crespo-Ribadeneyra, T. F. Headen, C. P. Grey and Q. Cai, *Energy Environ. Sci.*, 2020, **13**, 3469–3479.
15 Y. Morikawa, S. i. Nishimura, R. i. Hashimoto, M. Ohnuma and A. Yamada, *Adv. Energy Mater.*, 2020, **10**, 1903176.
16 H. Liu, P. Li, K. Fan, F. Lu, Q. Sun, Q. Zhang, B. Li, Y. Shu, L. Zong and L. Wang, *Angew. Chem.*, 2025, e202501307.
17 H. Kim, J. C. Hyun, D. H. Kim, J. H. Kwak, J. B. Lee, J. H. Moon, J. Choi, H. D. Lim, S. J. Yang and H. M. Jin, *Adv. Mater.*, 2023, **35**, 2209128.
18 L. Yuan, Q. Zhang, Y. Pu, X. Qiu, C. Liu and H. Wu, *Adv. Energy Mater.*, 2024, **14**, 2400125.
19 C. Jiang, Y. Li, C. Wan, Q. Wu, S. Yang, K. Chen, Y. You, Y. Tian, J. Huang and H. Xie, *Chem. Eng. J.*, 2025, 160124.
20 J. Lin, Q. Zhou, Z. Liao, Y. Chen, Y. Liu, Q. Liu and X. Xiong, *Angew. Chem., Int. Ed.*, 2024, **63**, e202409906.
21 B. Zhong, C. Liu, D. Xiong, J. Cai, J. Li, D. Li, Z. Cao, B. Song, W. Deng and H. Peng, *ACS Nano*, 2024, **18**, 16468–16488.
22 G. Zhang, C. Fu, S. Gao, H. Zhao, C. Ma, Z. Liu, S. Li, Z. Ju, H. Huo and P. Zuo, *Angew. Chem., Int. Ed.*, 2025, **64**, e202424028.
23 X. Feng, Y. Li, Y. Li, M. Liu, L. Zheng, Y. Gong, R. Zhang, F. Wu, C. Wu and Y. Bai, *Energy Environ. Sci.*, 2024, **17**, 1387–1396.
24 M. Li, Y. Wang, Y. Zhang and N. Zhang, *Chem. Eng. J.*, 2025, 160083.
25 P. Yu, W. Tang, F.-F. Wu, C. Zhang, H.-Y. Luo, H. Liu and Z.-G. Wang, *Rare Met.*, 2020, **39**, 1019–1033.
26 Y. Wang, M. Li, Y. Zhang and N. Zhang, *Chem. Eng. J.*, 2024, **499**, 156115.
27 Z. Tang, R. Zhang, H. Wang, S. Zhou, Z. Pan, Y. Huang, D. Sun, Y. Tang, X. Ji and K. Amine, *Nat. Commun.*, 2023, **14**, 6024.
28 K. Wang, F. Sun, H. Wang, D. Wu, Y. Chao, J. Gao and G. Zhao, *Adv. Funct. Mater.*, 2022, **32**, 2203725.
29 B. Wang, S. Zhang, X. Jia, F. Yuan, H. Sun, Z. Li, Q. Sun, Q. Wang and D. Zhang, *Chem. Eng. J.*, 2024, **499**, 156126.
30 J. Choi, M. E. Lee, S. Lee, H.-J. Jin and Y. S. Yun, *ACS Appl. Energy Mater.*, 2019, **2**, 1185–1191.
31 B. Zhang, C. M. Ghimbeu, C. Laberty, C. Vix-Guterl and J. m. Tarascon, *Adv. Energy Mater.*, 2016, **6**, 1501588.
32 X. X. He, W. H. Lai, Y. Liang, J. H. Zhao, Z. Yang, J. Peng, X. H. Liu, Y. X. Wang, Y. Qiao and L. Li, *Adv. Mater.*, 2023, **35**, 2302613.
33 X. Chen, J. Tian, P. Li, Y. Fang, Y. Fang, X. Liang, J. Feng, J. Dong, X. Ai and H. Yang, *Adv. Energy Mater.*, 2022, **12**, 2200886.
34 Z. Zheng, S. Hu, W. Yin, J. Peng, R. Wang, J. Jin, B. He, Y. Gong, H. Wang and H. J. Fan, *Adv. Energy Mater.*, 2024, **14**, 2303064.
35 X. Chen, Y. Fang, H. Lu, H. Li, X. Feng, W. Chen, X. Ai, H. Yang and Y. Cao, *Small*, 2021, **17**, 2102248.
36 Y. Li, Y. Lu, Q. Meng, A. C. Jensen, Q. Zhang, Q. Zhang, Y. Tong, Y. Qi, L. Gu and M. M. Titirici, *Adv. Energy Mater.*, 2019, **9**, 1902852.
37 D. A. Stevens and J. R. Dahn, *J. Electrochem. Soc.*, 2001, **148**, A803–A811.
38 J. R. Dahn, W. Xing and Y. Gao, *Carbon*, 1997, **35**, 825–830.
39 L. Li, D. Zhang, J. Deng, Y. Gou, J. Fang, H. Cui, Y. Zhao and M. Cao, *Carbon*, 2021, **183**, 721–734.
40 L. Xie, C. Tang, Z. Bi, M. Song, Y. Fan, C. Yan, X. Li, F. Su, Q. Zhang and C. Chen, *Adv. Energy Mater.*, 2021, **11**, 2101650.
41 A. Agrawal, S. Janakiraman, K. Biswas, A. Venimadhav, S. Srivastava and S. Ghosh, *Electrochim. Acta*, 2019, **317**, 164–172.
42 W. Chen, M. Wan, Q. Liu, X. Xiong, F. Yu and Y. Huang, *Small Methods*, 2019, **3**, 1800323.
43 D. Stevens and J. Dahn, *J. Electrochem. Soc.*, 2000, **147**, 1271.
44 O. Glatter, O. Kratky and H. Kratky, *Small angle X-ray scattering*, Academic Press, 1982.
45 P. Debye, H. Anderson and H. Brumberger, *J. Appl. Phys.*, 1957, **28**, 679–683.
46 P. E. Batson, *Phys. Rev. B: Condens. Matter Mater. Phys.*, 1993, **48**, 2608.
47 X. Chang, X. Zhou, X. Ou, C. S. Lee, J. Zhou and Y. Tang, *Adv. Energy Mater.*, 2019, **9**, 1902672.
48 Y. Lei, Q. Chen, P. Liu, L. Wang, H. Wang, B. Li, X. Lu, Z. Chen, Y. Pan and F. Huang, *Angew. Chem.*, 2021, **133**, 4755–4761.
49 G. Qian, J. Wang, H. Li, Z.-F. Ma, P. Pianetta, L. Li, X. Yu and Y. Liu, *Natl. Sci. Rev.*, 2022, **9**, nwab146.
50 D. Stevens and J. Dahn, *J. Electrochem. Soc.*, 2000, **147**, 4428.
51 C. M. Ghimbeu, J. Górka, V. Simone, L. Simonin, S. Martinet and C. Vix-Guterl, *Nano Energy*, 2018, **44**, 327–335.
52 E. P. Barrett and L. G. Joyner, *Anal. Chem.*, 1951, **23**, 791–792.
53 S. Al-Riyami, S. Ohmagari and T. Yoshitake, *Appl. Phys. Express*, 2010, **3**, 115102.

54 A. V. Sumant, P. Gilbert, D. S. Grierson, A. R. Konicek, M. Abrecht, J. E. Butler, T. Feygelson, S. S. Rotter and R. W. Carpick, *Diamond Relat. Mater.*, 2007, **16**, 718–724.
55 X. Zhou, S. Tunmee, T. Suzuki, P. Phothongkam, K. Kanda, K. Komatsu, S. Kawahara, H. Ito and H. Saitoh, *Diamond Relat. Mater.*, 2017, **73**, 232–240.
56 K. G. Latham, M. I. Simone, W. M. Dose, J. A. Allen and S. W. Donne, *Carbon*, 2017, **114**, 566–578.
57 D. Solomon, J. Lehmann, J. Kinyangi, B. Liang, K. Heymann, L. Dathe, K. Hanley, S. Wirick and C. Jacobsen, *Soil Sci. Soc. Am. J.*, 2009, **73**, 1817–1830.
58 F. Frati, M. O. Hunault and F. M. De Groot, *Chem. Rev.*, 2020, **120**, 4056–4110.
59 J. Zhao, X. X. He, W. H. Lai, Z. Yang, X. H. Liu, L. Li, Y. Qiao, Y. Xiao, L. Li and X. Wu, *Adv. Energy Mater.*, 2023, 2300444.
60 A. Ferrari and D. Basko, *Nat. Nanotechnol.*, 2013, **8**, 235–246.
61 M. S. Dresselhaus, G. Dresselhaus, R. Saito and A. Jorio, *Phys. Rep.*, 2005, **409**, 47–99.
62 K. Mori, J. Kim, S. Kubo and Y. Yamada, *J. Mater. Sci.*, 2022, **57**, 15789–15808.
63 N. Sun, J. Qiu and B. Xu, *Adv. Energy Mater.*, 2022, **12**, 2200715.
64 Y. Jiang and J. Liu, *Energy Environ. Mater.*, 2019, **2**, 30–37.
65 C. Bai, B. Li, C. Shu, W. Chen, Y. Han and D. Li, *Chem. Eng. J.*, 2025, **512**, 162207.
66 L. F. Zhao, Z. Hu, W. H. Lai, Y. Tao, J. Peng, Z. C. Miao, Y. X. Wang, S. L. Chou, H. K. Liu and S. X. Dou, *Adv. Energy Mater.*, 2021, **11**, 2002704.
67 P. Zhang, Y. Shu, B. Zhong, L. Yang and X. Guo, *Chem. Eng. J.*, 2024, **498**, 155231.
68 Y. Yuan, Z. Chen, H. Yu, X. Zhang, T. Liu, M. Xia, R. Zheng, M. Shui and J. Shu, *Energy Storage Mater.*, 2020, **32**, 65–90.
69 Y. Chen, F. Li, Z. Guo, Z. Song, Y. Lin, W. Lin, L. Zheng, Z. Huang, Z. Hong and M.-M. Titirici, *J. Power Sources*, 2023, **557**, 232534.
70 Y. Qian, S. Jiang, Y. Li, Z. Yi, J. Zhou, T. Li, Y. Han, Y. Wang, J. Tian and N. Lin, *Adv. Energy Mater.*, 2019, **9**, 1901676.
71 M. Reddy, M. Helen, A. Groß, M. Fichtner and H. Euchner, *ACS Energy Lett.*, 2018, **3**, 2851–2857.
72 X. Liu, M. Zhang, X. Wang, Y. Peng, Y. Liu, S. Ullah, Z. Duan, W. Gao, B. Song and M. Wei, *Adv. Mater.*, 2025, **37**, 2410673.
73 M. Salanne, B. Rotenberg, K. Naoi, K. Kaneko, P.-L. Taberna, C. P. Grey, B. Dunn and P. Simon, *Nat. Energy*, 2016, **1**, 1–10.
74 Z. Zhou, Z. Wang and L. Fan, *Chem. Eng. J.*, 2024, **490**, 151428.
75 G. Huang, H. Zhang, F. Gao, D. Zhang, Z. Zhang, Y. Liu, Z. Shang, C. Gao, L. Luo and M. Terrones, *Carbon*, 2024, 119354.